Research Article | Vol. 27, No. 5 | 4 Mar 2019 | OPTICS EXPRESS 6331

Optics EXPRESS

Radial sub-aperture coherence method to achieve beam steering with high precision and stability

C. WANG,[1,2] Z. PENG,[1] Y. LIU,[1] S. LI,[1,2] Z. ZHAO,[1,2] W. CHAN,[1,2] Q. WANG,[1,3] AND Q. MU[1,2,4]

[1]*State Key Laboratory of Applied Optics, Changchun Institute of Optics, Fine Mechanics and Physics, Chinese Academy of Sciences, Changchun, 130033, China*

[2]*Center of Material Science and Optoelectronics Engineering, University of Chinese Academy of Sciences, Beijing, 100049, China*

[3]*qdwang@ciomp.ac.cn*

[4]*muquanquan@ciomp.ac.cn*

Abstract: Sub-aperture coherence (SAC) algorithm, which is based on the classical phase modulation method called variable period grating (VPG), was usually used to control liquid crystal optical phased arrays (LCOPA) to achieve agile beam steering with high precision. However, the beam steering angle of SAC is severely affected by the beam aperture, which limits the generality of the algorithm distinctly. In this article, two kinds of new phase modulation method have been proposed to solve this problem, which were named as radial sub-aperture coherence (RSAC) and symmetrical radial sub-aperture coherence (SRSAC). By using RSAC, the holistic drift of steering angle, which is caused by the variation of beam aperture, can be effectively avoided. In addition, a series of equidistant steering points with ultra-high precision can be obtained. Upon this basis, SRSAC greatly enhances the steering angle's stability in the presence of system alignment error and relative vibration. Thus, the practicability of LCOPA for beam steering can be improved effectively.

1. Introduction

In recent years, with the rapid development of free-space optical (FSO) technology, the precision and stability of core beam steering device have become critical parameters that attract increasing attention in relevant field [1]. Meanwhile, the non-mechanical beam steering technology represented by LCOPA [2–5] can meet the performance requirements of FSO communication [6–8] and lidar [9,10] system in many aspects such as agile scan, low Size Weight and Power (SWaP) consumption [11]. On this basis, in order to achieve many specific applications such as high stability bidirectional laser communication and continuous tracking of dynamic target, the scanning accuracy of beam steering system need to be further enhanced.

The traditional phase control method for 1-D beam steering is VPG algorithm [12]. Since the phase delay that LCOPA can realize is quantized, the pointing accuracy of VPG decreases dramatically in some steering angle regions. Although the undesirable local pointing accuracy can be improved to a certain extent by the method of phase translation [13,14], the actual iterative calculation process may affect the overall dynamic response speed of the system. In 2014, SAC algorithm, a new phase control method introduced by Z. Tang and X. Wang, has effectively solved the problem of insufficient local pointing accuracy and greatly improved the scanning accuracy [15]. At present, although this modulation process can make the final pointing accuracy on the order of sub-mircoradian by the calibration of scanning points for the plane wave with a fixed aperture, the universal modulation method for arbitrary beam apertures with ultra-high precision and high stability is not particularly mature.

#352000 https://doi.org/10.1364/OE.27.006331
Journal © 2019 Received 15 Nov 2018; revised 1 Feb 2019; accepted 11 Feb 2019; published 20 Feb 2019

Optics EXPRESS

Taking into account the above factors, the LCOPA with two-dimensional pixel structure can be utilized for more flexible sub-aperture segmentation in order to improve the scanning accuracy substantially and ensure that the pointing accuracy is at an ultra-high level in the entire steering range. In this paper, two new phase modulation algorithms called RSAC and SRSAC are proposed for beam steering. Through RSAC, the minimum scanning interval of steering angles will be able to reach a level less than one micro-radian and eliminate local defects of pointing accuracy. Furthermore, an excellent resistance to the alignment error and slight vibration of the laser source can be obtained through SRSAC. The principles of the new algorithms will be firstly explained from a theoretical perspective, then the feasibility and practicability will be calculated by simulation, finally, the expected conclusion will be obtained by comparing the experimental data with the results of simulated analysis.

2. Theoretical principle

2.1 VPG and SAC algorithm

The ideal phase distribution of VPG, which is the most commonly used phase modulation algorithm for beam steering [12,16], is shown in Eq. (1).

$$\phi(x) = \mathrm{mod}\left(\frac{2\pi d}{\lambda}\cdot \mathrm{round}(x/d)\cdot\theta_{ideal}, 2\pi\right) \tag{1}$$

Whereλ is the wavelength of the modulated laser beam,θ_{ideal} is the desired steering angle, x is the position coordinate whose origin is the center of the phased array, d is the pitch of the pixel structure and the function mod(X, 2π) represents the modular operation of X. Actually, for the quantized phase gray levels, if the difference of adjacent phase gray level is assumed to be constant, the phase distribution with discretized gray levels will be rewritten as Eq. (2).

$$\phi_{GL}(x) = \frac{2\pi}{N_{gray}}\cdot \mathrm{round}(\frac{N_{gray}}{2\pi}\cdot\varphi(x)) \tag{2}$$

$\phi_{GL}(x)$ represents the correction of the phase distribution in Eq. (1) after considering the limited phase gray levels. The discontinuous phase value is one of the main reasons for the large pointing error in some local steering angle regions and the maximum pointing error can be estimated from Eq. (3).

$$\max(\theta_{error}) \approx \frac{\lambda}{N_{gray}L} \tag{3}$$

L represents the effective width of the modulator panel. If the actual beam aperture is less than the width of the modulator panel, apparently the value of L should be the former. According to the general hardware parameters and the wavelength of visible light, the maximum steering error can be calculated to be several micro-radians. One of the most intuitive examples is that if the desired steering angle input into the control program is set to be the maximum error angle in Eq. (3), the phase modulation at all points on the liquid crystal cell will be 0 according to Eq. (2), so the final output beam will not be loaded with any steering angle and deviates from the desired angle we set. The error with such magnitude in micro-radians will become the main error source of LCOPA beam steering, and other imperfections of the device, like fringe effect [17], cross talk [18,19] and laser induced effect [20–22] are secondary in terms of the contribution of the pointing error. To address the problem of decreasing pointing accuracy in these sick regions [13,23], if we can give up the points with larger error in the region and take two precise points in an external as the end points to carry out linear interpolation, a series of new high-precision steering points will be

Optics EXPRESS

obtained in the original sick region. Meanwhile, the resolution, also known as the scanning accuracy of the beam steering system, can be greatly improved and unified.

SAC provides a specific phase control method to realize above assumption without changing any hardware parameters of LCOPA. In original SAC, the working panel of LCOPA was divided into two rectangular phase modulation subdomains Σ_I and Σ_{II}, whose expected steering angle wereθ_I andθ_{II}, respectively [15]. The difference betweenθ_I andθ_{II} is a constant scanning step length, which is the optimal length of the scanning sections for modifying the sick region mentioned above, shown in Eq. (4) .

$$\theta_{step} = \theta_{II} - \theta_I \tag{4}$$

The widths of the two subdomains are L_I and L_{II}, and the occupation rates areη_I and η_{II}, shown in Eq. (5).

$$\eta_I = {L_I}/{L}, \eta_{II} = {L_{II}}/{L} \tag{5}$$

L is the total width of the panel, apparently $L = L_I + L_{II}$. If we adjust the proportion of the area of two subdomains so thatη_{II} changes from 0 to 1, the steering angle will change fromθ_I toθ_{II} equidistantly, which is beyond the reach of traditional VPG according to the previous error analysis.

2.2 RSAC algorithm

For some wavefront modulation system with varying aperture of the incident beam, SAC greatly reduces the pointing accuracy due to its limitation of lateral subdomain segmentation method. Even if the seriatim calibrations can be carried out for the incident beams with different apertures, the complexity of calibration data and the impact of unknown aperture errors are also inevitable. Fortunately, RSAC, which is a universal algorithm for the incident beams with arbitrary aperture, has been designed to replace SAC in this case. The modulation phase diagrams of SAC and RSAC are shown in Figs. 1(a) and 1(b), respectively.

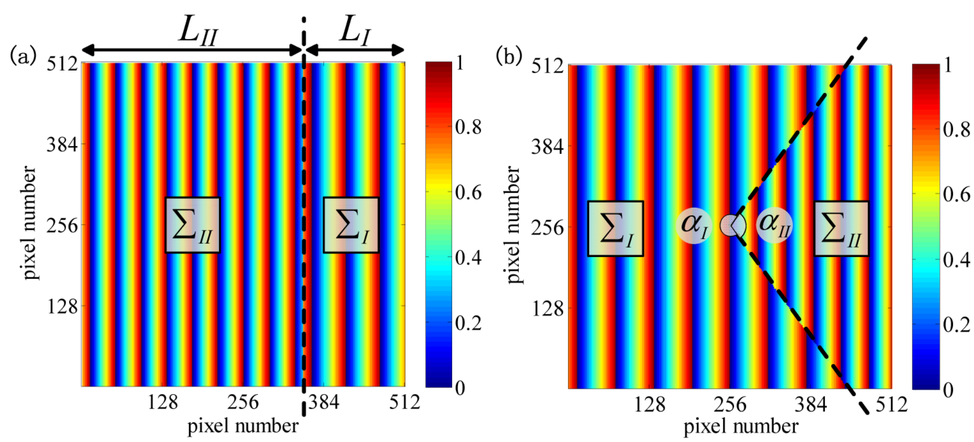

Fig. 1. Normalized phase diagrams of two sub-aperture algorithm. (a) SAC (b) RSAC

The light power in Σ_I and Σ_{II} is defined as Eq. (6).

$$P_I = \iint_{\Sigma_I} I(x,y)dxdy \, , P_{II} = \iint_{\Sigma_{II}} I(x,y)dxdy \tag{6}$$

It can be imagined that when the beam comes vertically into the center of LCOPA, for SAC, the proportion of P_I and P_{II} depends not only on the occupation rates of two subdomains, but also on the diameter and the energy distribution form of the beam. However, the aperture

Optics EXPRESS

segmentation lines of RSAC are along the radial direction and the occupation rates of two sectorial subdomains are proportional to their vertex angles, which are shown in Eq. (7).

$$\eta_I = {\alpha_I}/{2\pi}, \eta_{II} = {\alpha_{II}}/{2\pi} \tag{7}$$

Obviously, under the premise that the energy distribution of the incident beam is centrosymmetric, no matter how the beam diameter changes, Eq. (8) is always true, which is the advantage of RSAC over SAC.

$$P_I/(P_I + P_{II}) = \eta_I \text{ , } P_{II}/(P_I + P_{II}) = \eta_{II} \tag{8}$$

If the energy centroid of the diffracted light depends only on the value of P_I / P_{II} and is independent of the aperture of the incident light, the steering angle will be almost determined by the occupation rate because of the property shown in Eq. (8). In order to research the relationship between the steering angles and the occupation rates of subdomains, the normalized steering angle is defined in Eq. (9).

$$\theta_{norm} = \frac{\theta - \theta_I}{\theta_{II} - \theta_I} \tag{9}$$

In Eq. (9),θ is an actual steering angle in the scanning section [θ_I, θ_{II}). For simplicity, all the desired end points of the steering angles generated by VPG are integer multiples ofθ_{step} in this paper. The simulation curves betweenθ_{norm} andη_{II} with different beam apertures are shown in Figs. 2(a) and 2(b).

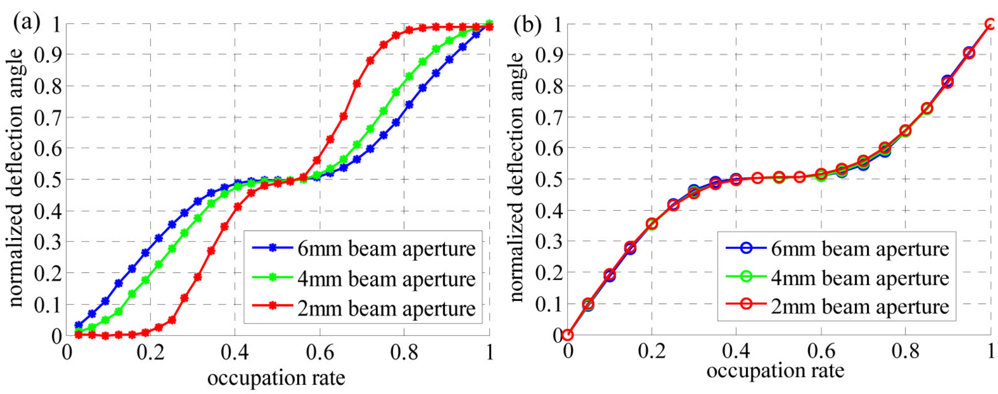

Fig. 2. Contrast diagram of θ_{norm} -η_{II} curves of two sub-aperture algorithms under different incident light aperture. (a) SAC (b) RSAC

The simulation parameters are selected according to the actual device parameters. The wavelength of incident light is 730nm, the pixel pitch of LCOPA is 15μm, and the number of pixels is 512 × 512. Considering that the weeny black matrix has little effect on beam steering accuracy, we approximately set the pixel width equal to the pixel pitch. On the other hand, although the defects of gamma correction and electronic noise also have some subtle effect on the pointing error of steering angles as a matter of fact, they do not affect the dependence ofθ_{norm} andη_{II} in a scanning section. So the deviation between the actual phase and the theoretical value is ignored and the reasonableness can be verified by subsequent experiments.

From Fig. 2, it can be seen that the scanning curves generated by RSAC are basically unchanged even though the aperture of incident light varies in a large range, which is impossible to realize with classic SAC. Furthermore, the scanning curves shown in Fig. 2(b)

Optics EXPRESS

are also quite insensitive to the changes of the main structural parameters of the system on the premise that θ_{step} is far less than the divergence angle (R_{out}) of the diffracted beam. Several other typical parameters were selected for simulation, such as d = 5~20μm, and the number of pixels is equal to 256 × 256, 1024 × 1024, etc. For incident light, the main parameters such as flat-top energy distribution or Gaussian energy distribution, visible or near-infrared, have little influence on the final scanning curve, either. Even the gray level changes caused by wavelength changes are carefully considered. Therefore, the scanning curve with such excellent stability in Fig. 2(b) is of great significance for error calibration or linear reconstruction of the occupation rate.

The purpose of linear reconstruction is to achieve the equidistant growth of the output steering angle in a scanning section. The specific procedure is dividing the simulated curve shown in Fig. 2(b) equidistantly according to the vertical coordinates and record a series of horizontal coordinates as a nonlinear reconstructed sequence of η_{II}, which is actually a process of sampling the inverse function of the scanning curve at regular intervals. The resultant sequence is made into a look-up table for actual beam steering. When the value of input desired angle is given by the driving program, the system will firstly work out the scanning section and the normalized angle, then obtain the accurate occupation rate by looking up the nonlinear sequence of η_{II} and generate the corresponding phase distribution.

2.3 SRSAC algorithm

In most processes of wavefront modulation, it is necessary to align the axis of the laser beam strictly with the center of the LCOPA panel. The alignment error between the LCOPA panel and the beam axis is also a common reason for the quality deterioration of the wavefront modulation. Therefore, for the specific application of high precision beam steering, SRSAC was designed as another new algorithm based on RSAC. The normalized phase distribution generated by SRSAC is shown in Fig. 3.

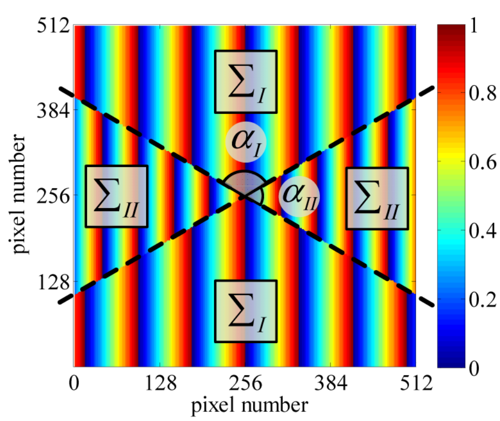

Fig. 3. Normalized phase diagram of SRSAC.

Different from the subdomains with single sector shape in RSAC, the subdomains in SRSAC present a symmetrical double-sector structure. The vertex angles of the sectorial subdomains vary from 0 to π, rather than from 0 to 2π. The new occupation rates of two subdomains are shown in Eq. (10).

$$\eta_I = \alpha_I / \pi, \eta_{II} = \alpha_{II} / \pi \tag{10}$$

This symmetrical structure can effectively reduce the steering angle error caused by the alignment error between the beam axis and the center of the LCOPA panel. The concrete principle is shown in Fig. 4.

Optics EXPRESS

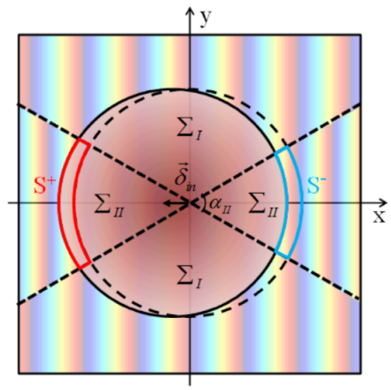

Fig. 4. Schematic diagram of alignment error based on SRSAC.

The circular region in Fig. 4 represents the cross section of the laser beam. Assuming that there is a translation along x direction between the position of the beam cross section and its desired central position, which is defined as$\boldsymbol{\delta_{in}} = (\delta_{in,x}, \delta_{in,y})$, it is not difficult to find that the main area variation of the beam cross section in Σ_{II} can be divided into S^+ and S^-. When the value of$\delta_{in,y}$ approaches 0, the areas of S^+ and S^- are shown in Eqs. (11a) and (11b), respectively.

$$S^+ = 2R\sin\left(\alpha_{II}/2\right)\cdot\delta_{in,x} + O(\delta_{in,x}{}^2) \tag{11a}$$

$$S^- = 2R\sin\left(\alpha_{II}/2\right)\cdot\delta_{in,x} - O(\delta_{in,x}{}^2) \tag{11b}$$

Where R is the effective radius of the beam section and $O(\delta_{in,x}{}^2)$ is the second order small quantity of$\delta_{in,x}$ .Therefore, the energy variation in Σ_{II} can be calculated in Eq. (12).

$$\lim_{\delta_{in,x}\to 0}\Delta P_{II} = \lim_{\delta_{in,x}\to 0}\left(S^+ - S^-\right)\cdot I\left(R\right) = O(\delta_{in,x}{}^2) \tag{12}$$

It can be inferred that the partial differential of the power in each subdomain satisfies Eq. (13a).

$$\frac{\partial P_{II}}{\partial\delta_{in,x}} = 0, \frac{\partial P_I}{\partial\delta_{in,x}} = \frac{\partial(P - P_{II})}{\partial\delta_{in,x}} = 0 \tag{13a}$$

When the alignment error exists only in y direction, a conclusion similar to Eq. (13a) can be obtained, as shown in Eq. (13b).

$$\frac{\partial P_I}{\partial\delta_{in,y}} = 0, \frac{\partial P_{II}}{\partial\delta_{in,y}} = \frac{\partial(P - P_I)}{\partial\delta_{in,y}} = 0 \tag{13b}$$

It is obvious that the powers within two subdomains are first order differentiable functions at the origin of coordinates, which satisfy the total differential relations in Eqs. (14a) and (14b).

$$dP_I = \frac{\partial P_I}{\partial\delta_{in,x}}d\delta_{in,x} + \frac{\partial P_I}{\partial\delta_{in,y}}d\delta_{in,y} = 0 \tag{14a}$$

$$dP_{II} = \frac{\partial P_{II}}{\partial\delta_{in,x}}d\delta_{in,x} + \frac{\partial P_{II}}{\partial\delta_{in,y}}d\delta_{in,y} = 0 \tag{14b}$$

Optics EXPRESS

The significance of Eq. (14) is that when the magnitude of the alignment error vector is much smaller than the radius of the spot, the power falling within each subdomain can be kept stable regardless of the direction in which the vector of the alignment error points. The stability of the power ratio in two subdomains will guarantee the stability of the final steering angle. Although in the process of coherent superposition of two sub-beams, the power proportion of the sub-beams cannot strictly determine the position of the energy centroid of the interference field, it can be inferred from the subsequent simulation that the influence of the small phase-shift can be neglected.

3. Simulated analysis of steering angle error

3.1 Evaluation of angular error caused by the variation of beam aperture

Based on the previous theoretical analysis, the relation between the RMS of normalized steering angle error and the apertures of the incident beam is simulated in a scanning section with the length ofθ_{step}, as shown in Fig. 5. It is assumed that the control program is calibrated according to the scanning angle sequence when the incident beam aperture is 6mm.

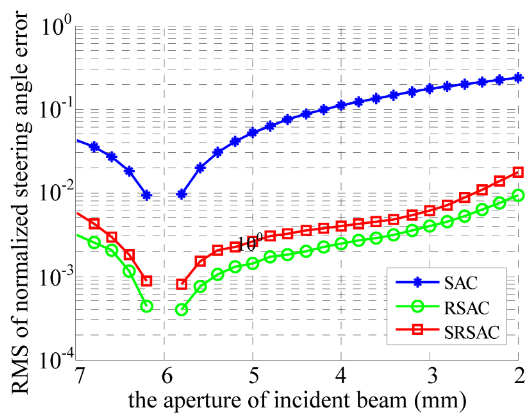

Fig. 5. Simulation diagram of the relationship between the RMS of normalized steering angle error and the beam aperture.

The RMS of the normalized steering angle error in Fig. 5 means the ratio between the RMS of actual steering angle error andθ_{step} . It can be seen that the steering angle error of RSAC and SRSAC caused by the variation of beam aperture is almost within θ_{step} /100 and can be completely ignored compared to that of SAC.

3.2 Tolerance analysis of the alignment error

In order to study the concrete magnitude of the steering angle deviation caused by the alignment error, several 2-D surfaces representing the relationship of them are simulated. The simulation of RSAC error surface is carried out in order to compare it with SRSAC and show the stability of the latter. Figures 6-9 show the error surfaces when the beam aperture is 6mm and the occupation rates are taken as several discrete values.

Optics EXPRESS

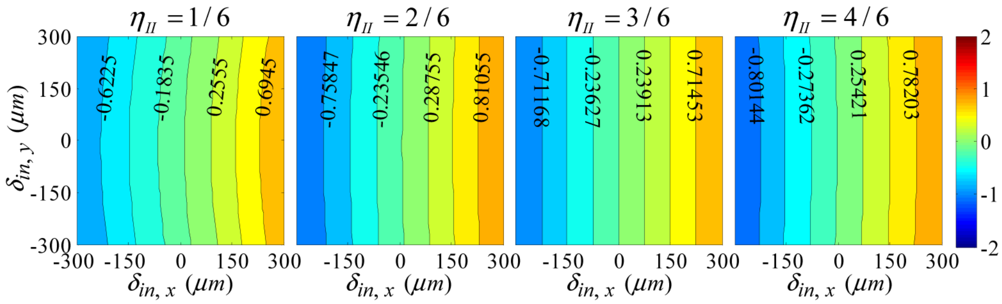

Fig. 6. The x-direction output error surface (μrad) based on RSAC.

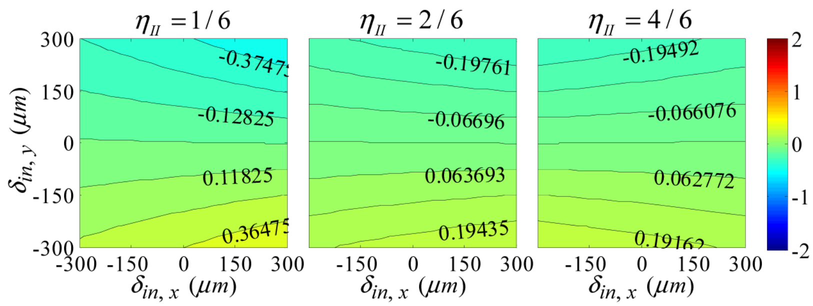

Fig. 7. The y-direction output error surface (μrad) based on RSAC.

In Figs. 6 and 7, either in x or y direction, the output error surface withη_{II} = 4/6 is similar to that withη_{II} = 2/6, but the trend of contour bending is symmetrical. The similar symmetry also exists between the contours of the output error surfaces withη_{II} = 1/6 andη_{II} = 5/6, so the surface withη_{II} = 5/6 is omitted. The y-direction output error surfaces withη_{II} = 3/6 are also removed because the output error of all the points is zero. Two key conclusions can be obtained from the output error simulation of RSAC.

1) The x-direction output error contours are approximated to some equidistant straight lines, which means that$\delta_{out,\,x}$ can be regarded as being linearly related to$\delta_{in,\,x}$ but independent of$\delta_{in,\,y}$.

2) In most of the defined range of$\boldsymbol{\delta_{in}}$, the y-direction output error of large-aperture laser beam is less than 0.2μrad, whose magnitude is acceptable. So the emphasis of the subsequent analysis will be mainly on the output error in x-direction.

The output error surfaces based on SRSAC are shown in Figs. 8 and 9, whose contour variation trends are completely different from those based on RSAC.

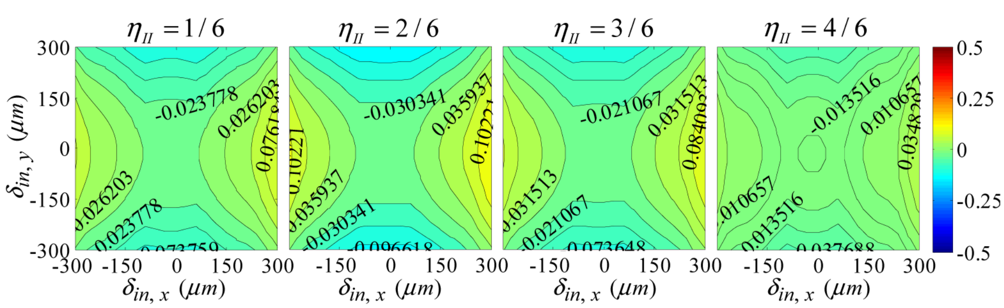

Fig. 8. The x-direction output error surface (μrad) based on SRSAC.

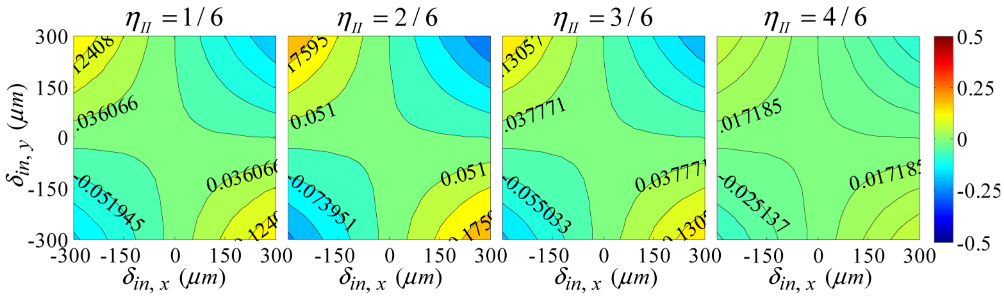

Fig. 9. The y-direction output error surface (μrad) based on SRSAC.

In Figs. 8 and 9, there is no phenomenon of a certain contour crossing the origin of coordinates, which is consistent with the conclusion shown in Eq. (13). Finally, the overall RMS of the normalized steering angle error in x-direction affected by the alignment error is given by Fig. 10. It can be seen that the negligible magnitude (θ_{step} /1000) of the x error based on SRSAC is much smaller than that on SAC and RSAC in the whole defined input error space$\boldsymbol{\delta_{in}}\in(-0.3\text{mm}, 0.3\text{mm})^2$, which shows that SRSAC has much better stability than SAC and RSAC in the presence of the system alignment error.

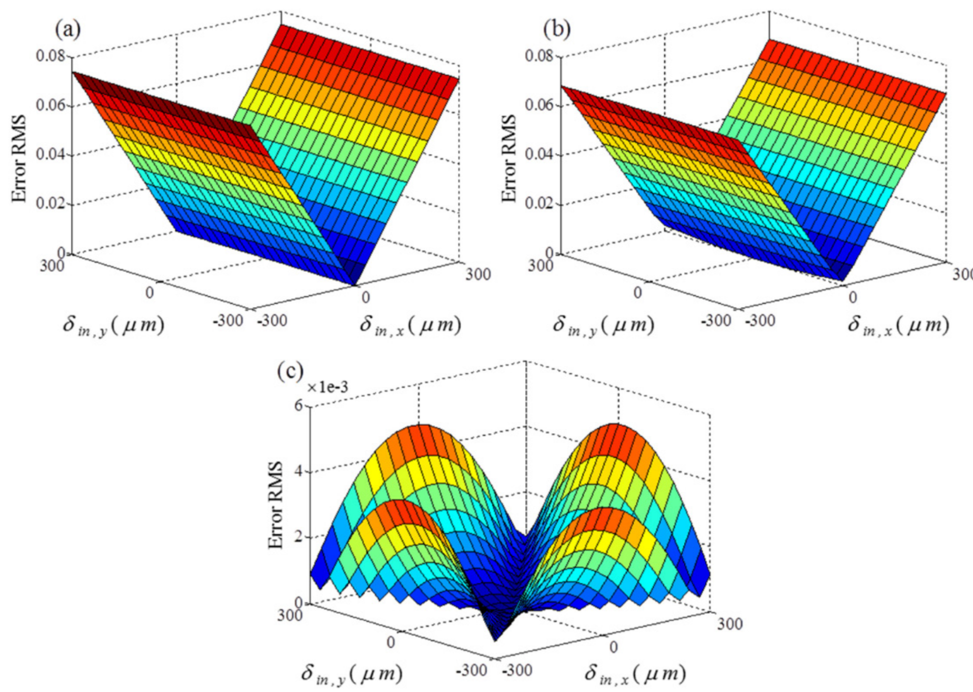

Fig. 10. Simulation diagram of the RMS of normalized steering angle error in x-direction with different alignment error. (a) SAC (b) RSAC (c) SRSAC

In addition, the analogue simulation of other apertures of the incident light is also performed, which shows that for the same alignment error and occupation rate, the steering angle error will increase inversely with the decrease of incident light aperture. According to the theory of Fourier optics, the relative angle errorθ_{error} / R_{out} , as another common form of steering angle error definition [13], will remain stable as the aperture of the incident light changes.

Optics EXPRESS

3.3 Analysis of the wavefront deformation effect

Unlike traditional VPG, the wavefront of the beam deflected by the algorithms we proposed must be deformed to a certain extent compared with the incident wavefront, which is not expected in the beam steering process. Considering simply in terms of optical aberration, our algorithms is actually a process of realizing new tilts by using the weighted average of two original tilts. In theory, it is inevitable that other aberrations will be introduced, but what is the order of magnitude of these aberrations apart from the tilt? For analyzing the problem quantitatively, Zernike polynomial expansion method can be used to calculate the size of additional aberrations. In the case of SRSAC, a particular phase distribution can be imagined for residual aberration analysis, where$\theta_I = 0$ and$\theta_{II} = \theta_{step}$. All other phase distributions with equal occupation rates can be considered as the superposition of this particular phase distribution and pure tilts. The first 20 items of Zernike coefficient distribution with several typical occupation rates are shown in Fig. 11, where R = 6mm,θ_{step} = 10μrad and λ = 0.73μm.

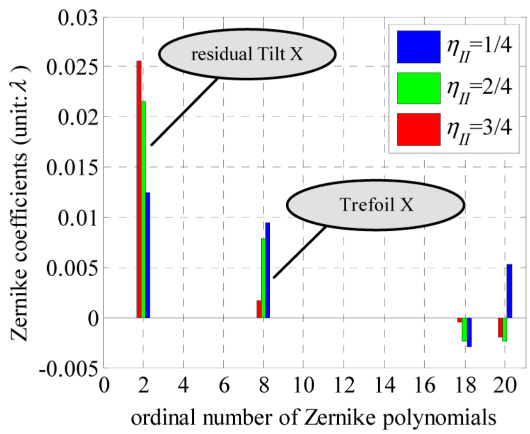

Fig. 11. Schematic diagram of Zernike coefficients of the accessary aberration.

In addition to the residual tilt X, it can be seen that the main aberration attached to SRSAC is Trefoil X, whose order of magnitude is no more than 1% of the wavelength. The non-tilt aberrations carried by the deflected beams are extremely small that the effects of these aberrations on the beam energy distribution and wavefront shape are negligible even after long distance propagation.

This effect can also be considered from the divergence angle R_{out}, which equals to$\lambda/(\pi R)$ according to the principle of Fourier transform. Theoretically, $R \times \theta_{step}$ directly reflects the size of the accessary aberration and must be far smaller than the wavelength on the premise of $\theta_{step} << R_{out}$. Hence trying to ensure such a great suppression of non-tilt aberration is another mean reason why we set the magnitude difference betweenθ_{step} and R_{out} .

4. Experimental validation of RSAC and SRSAC algorithm

4.1 Experimental set-up for fine measurement

The schematic and physical diagrams of the optical system for steering angle measurement are shown in Figs. 12 and 13, respectively.

Optics EXPRESS

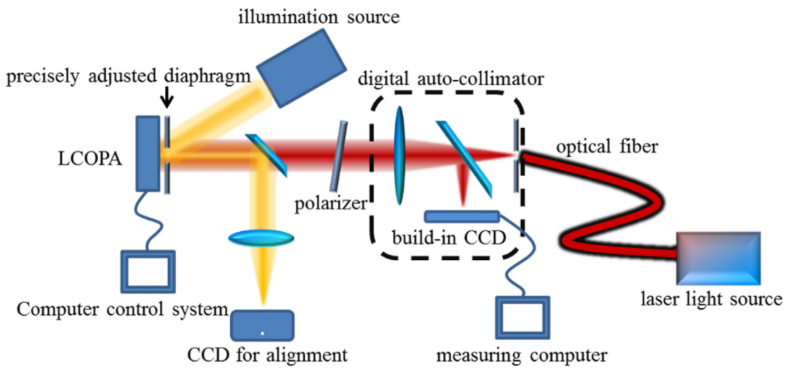

Fig. 12. Schematic diagram of high precision measuring system.

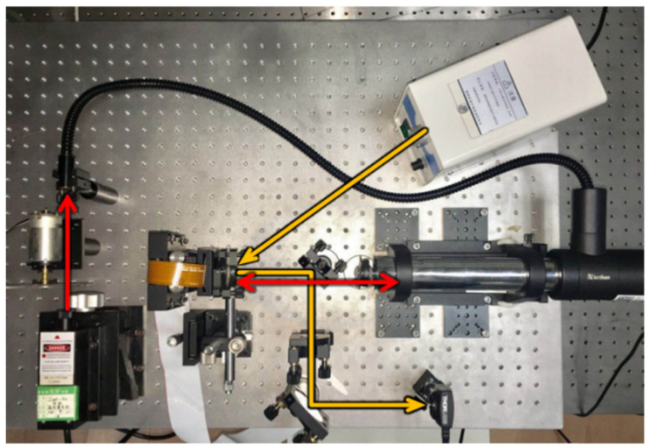
Fig. 13. Actual measuring system.

The laser with wavelength of 730*nm* enters digital auto-collimator by fiber-optic coupling. The digital auto-collimator, an integrated commercial instrument for angle measuring, emits large aperture plane wave and focuses the reflected light on the built-in CCD. Its focus system has a focal length of 300mm and the pixel pitch of the built-in CCD is 5.2µm. The system accurately captures the position of the cross-shaped spot and works out its deviation from the reference zero point by local centroid algorithm. Figure 14 shows several high-precision measurement interfaces.

Optics EXPRESS

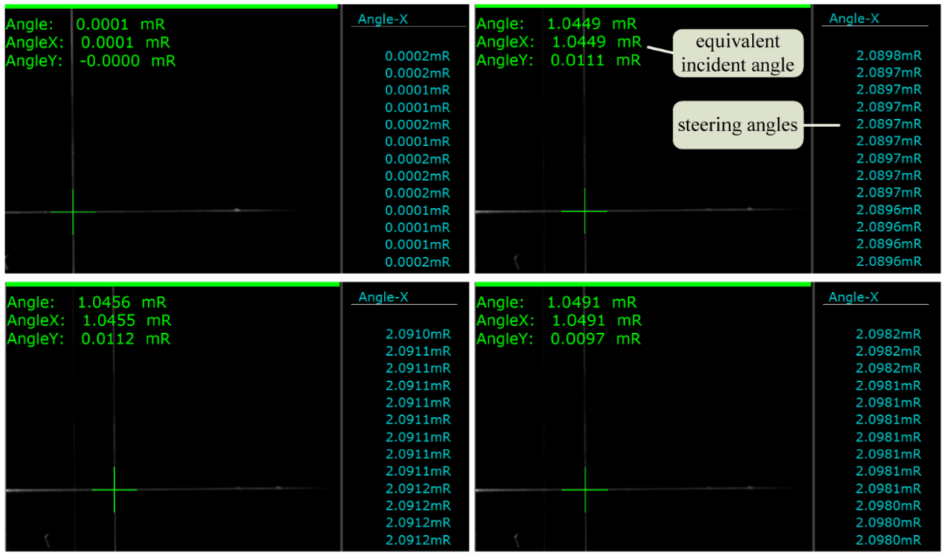

Fig. 14. Continuous measurement interface of reference zero error and steering angles.

Moreover, a diaphragm, whose position can be adjusted with high precision in the horizontal and vertical direction, is placed close to the panel of the LCOPA. So it is possible to be equivalent to the beams with different cross-section radius and alignment errors by adjusting the aperture and the position of the diaphragm. In order to determine whether the position of the diaphragm is accurate, a lateral illumination system shown with the yellow beam in Figs. 13 is introduced to make the diaphragm and modulator panel clearly imaged on the alignment CCD, so that the displacement platform with diaphragm can be fine-tuned by observing the imaging situation.

4.2 Precision and stability test of RSAC algorithm

In order to evaluate the consistency between the measured discrete points with the simulatedθ_{norm} -η_{II} curve, an approximate mathematical formula for simulated scanning curve should be established as a target function of regression analysis. Considering the conciseness and accuracy of the formula, an approximate piecewise power function is established for the nonlinear scanning curve of RSAC, as shown in Eq. (15).

$$\tilde{F}_{\delta_C}(x) = \begin{cases} \left(-2^{3/2+3\delta_C}(1/2-x)^{5/2+3\delta_C}+1/2\right)\cdot\left(1+2\delta_c\right) & x \le 1/2 \\ \left(2^{3/2-3\delta_C}(x-1/2)^{5/2-3\delta_C}-1/2\right)\cdot\left(1-2\delta_c\right)+1 & x > 1/2 \end{cases} \qquad (15)$$

Equation (15) contains a variable parameterδ_c for one dimensional regression analysis of subsequent experimental data, which represents the deviation of normalized steering angle fromθ_{norm} = 0.5 when the alignment error exists andη_{II} = 0.5. As explained earlier, with the premise that$\theta_{step} << R_{out}$, the form of the scanning curve will be extremely insensitive to the structure parameters of the modulator and the wavelength of the laser beam. So Eq. (15) does not contain any other parameters related to the diffraction system. An intuitive comparison between the simulated scanning curves and the corresponding approximate formulas in the presence of different alignment errors is shown in Fig. 15.

Optics EXPRESS

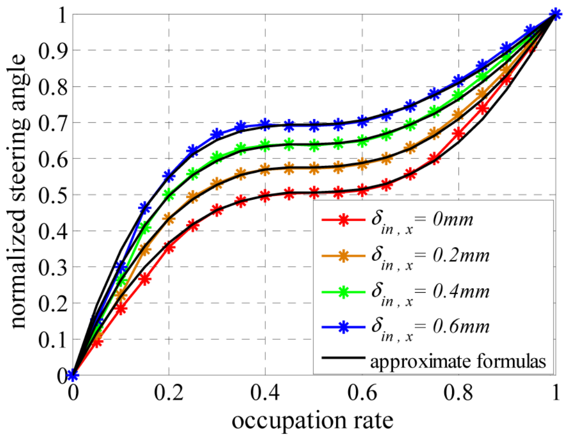

Fig. 15. The contrast diagram of RSAC simulated scanning curves and their approximate formulas.

A scanning section withθ_{step} = 10μrad is randomly selected in the overall scanning range during the measurement. Without the error of alignment, three sets of normalized experimental data are obtained by adjusting the aperture size of the diaphragm, as shown in Fig. 16.

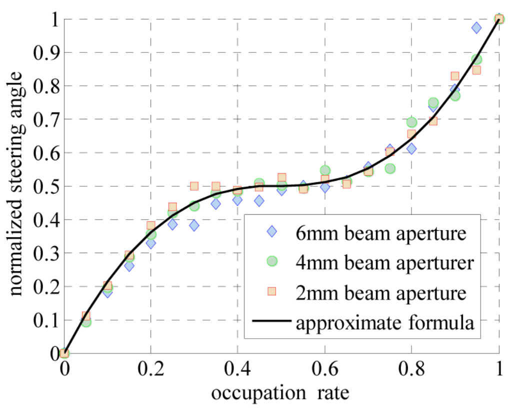

Fig. 16. The contrast diagram of RSAC scanning curves with different beam apertures.

The absence of alignment error meansδ_c = 0, and Eq. (15) can be simplified to Eq. (16).

$$\tilde{F}_{\delta_c=0} = 2\sqrt{2}\,\mathrm{sgn}(x-0.5)\cdot\left|x-0.5\right|^{5/2}+0.5 \tag{16}$$

Taking Eq. (16) as the theoretical value, the RMS of residual error with different beam apertures are all less than 0.25μrad. Considering that the RMS of the inherent measuring error fluctuation is estimated to be 0.2μrad, it can be inferred that the deviation between the measured data and the simulated nonlinear curve is mainly composed of random measurement error, while the actual systematic error can be ignored.

In the presence of alignment errors, the actual measurement point will move up or down as a whole, shown in Fig. 17.

Optics EXPRESS

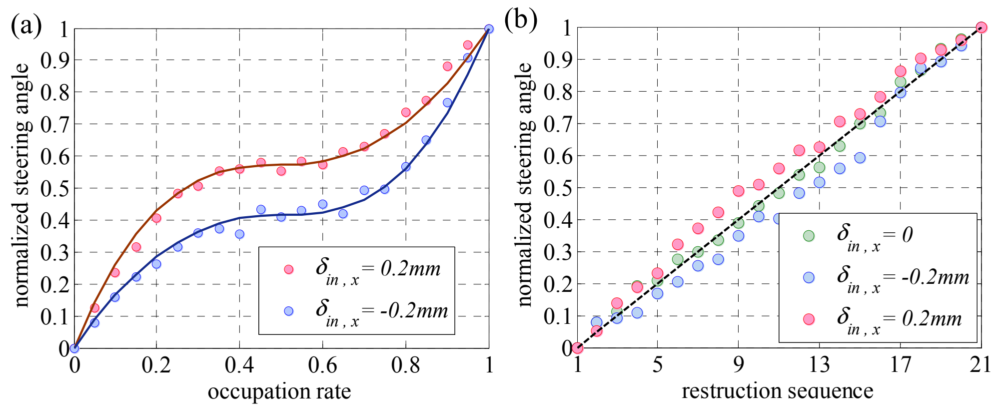

Fig. 17. Schematic diagram of the RSAC measured angles. (a) The normalized steering angle sequences before linearized reconstruction and their custom fitting curves. (b) The normalized steering angle sequences after linearized reconstruction and the desired straight line.

The single parameter fitting analysis of the measured angles in Fig. 15(a) is carried out by using Eq. (15) and the fitting results are shown in Table 1.

Table 1. The statistical parameters of RSAC data error with $\delta_{in,x} = \pm 0.2mm$.

$\delta_{in,x}$ (mm)	+ 0.2	−0.2
δ_c	0.072	−0.083
R-square	0.987	0.985
residual error RMS(μrad)	0.22	0.23

Based on the simulation results shown in the third diagram of Fig. 6, it can also be roughly estimated that δ_c should be about ± 0.064 in the above fitting result. The slight difference between simulation results and fitting results may be caused by the inaccuracy of the aperture of the diaphragm. However, the overall trend of the actual measurement data is generally consistent with the results predicted by the simulation analysis.

Applying the linearized reconstruction principle, the relationship between the normalized steering angle and the subscript of the reconstructed occupation sequence is shown in Fig. 17(b). It can be seen that the overall upward or downward movement of data points cannot be eliminated if the alignment errors do exist.

4.3 Precision and stability test of SRSAC algorithm

The θ_{norm} -η_{II} curve of SRSAC is completely different from that of RSAC. In fact, by analyzing the phase distribution of these two algorithms, it can be inferred that in the absence of alignment error, the scanning curve of SRSAC can be obtained by magnifying the front half of the RSAC curve proportionately. So the approximate formula for the scanning curve of SRSAC is shown in Eq. (17) and Fig. 18.

$$\tilde{F}^{s}(x) = 2\tilde{F}_{\delta_C=0}(x/2) = -(1-x)^{5/2} + 1 \qquad (17)$$

Research Article Vol. 27, No. 5 | 4 Mar 2019 | OPTICS EXPRESS 6345

Optics EXPRESS

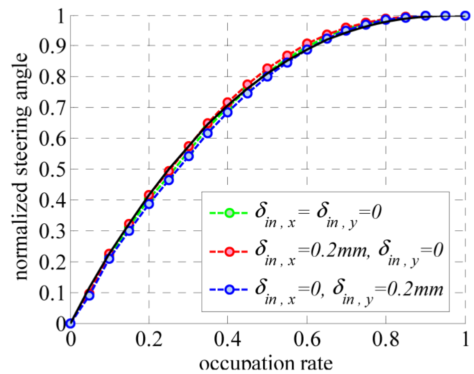

Fig. 18. The contrast diagram of SRSAC simulated curves and their approximate formula.

Considering the error surfaces shown in Fig. 8 are similar to saddle surfaces, two curves whose alignment error vectors are respectively along x and y axis actually have the largest deviation in all curves with the same $|\boldsymbol{\delta}_{in}|$. Nevertheless, this largest deviation is apparently negligible in Fig. 18, so that we can use Eq. (17) to approximate the θ_{norm} -η_{II} curve with any alignment error in the simulated range, which also proved that SRSAC has excellent stability in the presence of alignment errors. The measured data of SRSAC is shown in Fig. 19.

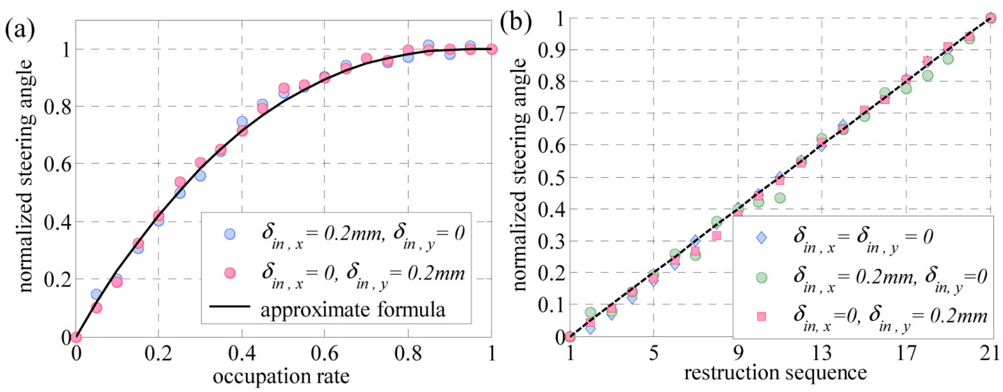

Fig. 19. Schematic diagram of the SRSAC measured angles. (a) The normalized steering angle sequences before linearized reconstruction and their custom fitting curves. (b) The normalized steering angle sequences after linearized reconstruction and the desired straight line.

Comparing with Fig. 17(b), the reconstructed sequences of SRSAC shown in Fig. 19(b) will not move upward or downward as a whole due to the alignment error, which provides a powerful guarantee for realizing ultra-high scanning accuracy and the excellent equidistant property of the steering angles. Concerned about the measurement accuracy of the experimental devices, the minimum scanning interval of RSAC and SRSAC is controlled at 0.5μrad. Theoretically, a higher scanning accuracy can be achieved by increasing the number of sample points of reconstructed sequences within a scanning section, if the measurement accuracy restriction of the verification experiment is not considered.

5. Conclusion

In this paper, two new LCOPA control methods are designed basing on SAC. RSAC can effectively reduce the influence of the beam aperture variation on the steering angle for centrosymmetric incident beams. On this basis, we retain the advantages of RSAC and successfully design SRSAC which can maintain wonderful stability in the presence of alignment errors. Ultimately, the precision requirements of the device mounting position and

Optics EXPRESS

the limits on the amplitude of environmental vibration can be greatly reduced by using SRSAC. Under the influence of macroscopic aperture variation and alignment error, the SRSAC steering angle error can be restrained within θ_{step} / 100.

Although the pointing accuracy of RSAC and SRSAC do not make a noticeable improvement over that of VPG in most of the locations within the scanning range because the end points of the scanning section (η_{II} = 0 or 1) are still implemented based on VPG, these new methods can effectively patch the pointing accuracy problem of a few scattered sick regions. Furthermore, after splicing all small scanning sections together, these two algorithms can easily reduce the expectation of the minimum scanning interval angle to the order of sub-micro radians on the basis of maintaining the equidistant property of the steering angle sequences, which allows the scanning system to obtain an explicit and stable ultra-high resolution across the full scanning range.

In all probability, the high precision 1D steering principle of these algorithms will have great potential to be extended to 2D steering, which will take it one step further to enhance the practicability and competitiveness in the field of FSO communication and lidar.

Funding

National Natural Science Foundation of China (11604327, 11174274, 11174279, 61205021 and 11204299); Science Foundation of State Key Laboratory of Applied Optics.

Acknowledgments

This work was supported by the National Natural Science Foundation of China and State Key Laboratory of Applied Optics, Changchun Institute of Optics, Fine Mechanics and Physics, Chinese Academy of Sciences.

References

1. P. F. McManamon, T. A. Dorschner, D. L. Corkum, L. J. Friedman, D. S. Hobbs, M. Holz, S. Liberman, H. Q. Nguyen, D. P. Resler, R. C. Sharp, and E. A. Watson, "Optical phased array technology," Proc. IEEE **84**(2), 268–298 (1996).
2. Z. Zhang, Z. You, and D. Chu, "Fundamentals of phase-only liquid crystal on silicon (LCOS) devices," Light Sci. Appl. **3**(10), e213 (2014).
3. D. Vettese, "Liquid crystal on silicon," Nat. Photonics **4**(11), 752–754 (2010).
4. Z. Zhang, A. M. Jeziorska-Chapman, N. Collings, M. Pivnenko, J. Moore, B. Crossland, D. P. Chu, and B. Milne, "High quality assembly of phase-only Liquid Crystal on Silicon (LCOS) devices," J. Disp. Technol. **7**(3), 120–126 (2011).
5. A. Choubey, F. Andros, and B. Sammakia, "Study of assembly processes for liquid crystal on silicon (LCoS) microdisplays," IEEE Trans. Compon. Packag. Tech. **28**(2), 303–310 (2005).
6. Y. Lin, M. Mahajan, D. Taber, B. Wen, and B. Winker, "Compact 4 cm aperture transmissive liquid crystal optical phased array for free-space optical communications," Proc. SPIE **5892**(3077), 58920C (2005).
7. B. Winker, M. Mahajan, and M. Hunwardsen, "Liquid crystal beam directors for airborne free-space optical communications," Aerospace Conference, Proc. IEEE Vol.**3**, 1702 (2004)
8. W. J. Miniscalco and S. A. Lane, "Optical space-time division multiple access," J. Lightwave Technol. **30**(11), 1771–1785 (2012).
9. Y. Wang and M. C. Wu, "An optical phased array for LIDAR," J. Phys. Conf. Ser. **772**(1), 012004 (2016).
10. N. L. Seldomridge, J. A. Shaw, and K. S. Repasky, "Dual-polarization lidar using a liquid crystal variable retarder," Opt. Eng. **45**(10), 106202 (2006).
11. X. Wang, L. Wu, X. He, X. Huang, and Q. Tan, "Theoretical analysis on power stability and switch time of the non-mechanical beam steering using liquid crystal optical phased array," Liq. Cryst. **45**(10), 1477–1486 (2018).
12. P. F. McManamon, P. J. Bos, M. J. Escuti, J. Heikenfeld, S. Serati, H. Xie, and E. A. Watson, "A review of phased array steering for narrow-band electrooptical eystems," Proc. IEEE **97**(6), 1078–1096 (2009).
13. D. Engström, J. Bengtsson, E. Eriksson, and M. Goksör, "Improved beam steering accuracy of a single beam with a 1D phase-only spatial light modulator," Opt. Express **16**(22), 18275–18287 (2008).
14. L. Kong, Y. Zhu, Y. Song, and J. Yang, "Beam steering approach for high-precision spatial light modulators," Chin. Opt. Lett. **8**(11), 1085–1089 (2010).
15. Z. Tang, X. Wang, Z. Huang, Q. Tan, Y. Duan, G. Suo, J. Du, and Q. Qiu, "Sub-aperture coherence method to realize ultra-high resolution laser beam deflection," Opt. Commun. **335**, 1–6 (2015).
16. K. Van Acoleyen, W. Bogaerts, J. Jágerská, N. Le Thomas, R. Houdré, and R. Baets, "Off-chip beam steering with a one-dimensional optical phased array on silicon-on-insulator," Opt. Lett. **34**(9), 1477–1479 (2009).

Optics EXPRESS

17. E. Haellstig, J. Stigwall, M. Lindgren, and L. Sjoqvist, “Laser beam steering and tracking using a liquid crystal spatial light modulator,” Proc. SPIE **5087**(10), 13 (2003).
18. A. Linnenberger, S. Serati, and J. Stockley, “Advances in optical phased array technology,” Proc. SPIE **6304**(2), 268–298 (2006).
19. H. Yang, B. Robertson, D. Yu, Z. Zhang, and D. P. Chu, “Origin of transient crosstalk and its reduction in phase-only LCOS wavelength selective switches,” J. Lightwave Technol. **31**(23), 3822–3829 (2013).
20. X. He, X. Wang, L. Wu, Q. Tan, M. Li, J. Shang, S. Wu, and Z. Huang, “Theoretical modeling on the laser induced effect of liquid crystal optical phased beam steering,” Opt. Commun. **382**, 437–443 (2017).
21. I. C. Khoo and S. L. Zhuang, “Nonlinear optical amplification in a nematic liquid crystal above the Frederiks transition,” Appl. Phys. Lett. **37**(1), 3–4 (1980).
22. E. Santamato, G. Abbate, P. Maddalena, L. Marrucci, and Y. R. Shen, “Laser-induced nonlinear dynamics in a nematic liquid-crystal film,” Phys. Rev. Lett. **64**(12), 1377–1380 (1990).
23. D. Engström, J. Bengtsson, E. Eriksson, and M. Goksör, “Steering accuracy of a spatial light modulator-based single beam steerer: guidelines and limitations,” Proc. SPIE **7038**, 703829 (2008).